


Cite this: *J. Mater. Chem. A*, 2022, 10, 2055

Potassium-ion storage behavior of microstructure-engineered hard carbons†

Hoseong Kim,^a Jong Chan Hyun,^b Ji In Jung,^a Jin Bae Lee,^c Jaewon Choi,^d Se Youn Cho,^e Hyung-Joon Jin^{*af} and Young Soo Yun ^{*bg}

The staging of potassium-ion intercalation reactions with graphite-like carbon materials has been previously chronicled; however, the potassium-ion storage behavior of disordered graphitic carbons (DGCs) has not been elucidated owing to their complex microstructures and the lack of systematic studies. In this study, microstructure-engineered DGCs were prepared using natural polymers by simple pyrolysis, followed by high-temperature annealing from 1200 °C to 2800 °C, and their potassium-ion storage properties were investigated and compared with their lithium-ion storage characteristics. In contrast to the lithium-ion intercalation reactions, which are dependent on local graphitic ordering, the stage I potassium-ion intercalation reaction was found to occur in highly disordered graphitic structures with a few nanometer-sized graphitic domains and an expanded *d*-spacing of >3.5 Å. In addition, the potassium-ion intercalation reactions with the highly expanded graphitic lattices were considerably faster and more stable compared to those with the highly developed disordered graphitic structures. These results suggest that hard carbons with a loosely packed disordered graphitic structure can be employed as effective high-performance anode materials for potassium-ion batteries.

Received 19th October 2021
Accepted 25th December 2021

DOI: 10.1039/d1ta08981a

rsc.li/materials-a

Introduction

Potassium-ion batteries (PIBs) have recently been spotlighted as next-generation energy storage devices, particularly for use in large-scale grid systems and power sources for mass-scalable electronic devices, owing to the various advantages of potassium-ion charge carriers such as high redox activity, resource availability, and chemical properties similar to those of the well-understood lithium ions.^{1–3} Extensive research has been conducted on key materials for applications in battery components such as electrolytes,^{4–8} cathodes,^{9–15} and anodes.^{16–31} In particular, various carbon-based materials have been investigated as anode materials for PIBs to meet the urgent need for feasible anode materials with high electrochemical

performance. Potassium ions can form stable potassium-ion-graphite intercalation compounds through phase reactions *via* KC₄₈, KC₃₆, KC₂₄, and KC₈, where a large potassium ion (~3 Å in diameter) can be inserted in every graphene sheet, leading to a considerable expansion of each graphene lattice up to 5.35 Å.³² However, the large volume change fatally damages the solid electrolyte interface (SEI) layers, resulting in poor cycling stability.³³ In addition, the intercalation reaction suffers from sluggish solid-state diffusion kinetics of potassium ions in the internal structure of graphite.³⁴ These hindrances limit the use of graphite-like ordered carbon materials as PIB anodes despite their high theoretical capacity of ~279 mA h g⁻¹ and low redox potential of ~0.1 V. Accordingly, defective carbon materials, including pseudocapacitive heteroatoms, have been examined as alternatives because of their mass-scalability, tunable material properties, and superior electrochemical performances compared with those of graphite-like materials.³⁵ However, these pseudocapacitive carbon materials also induce critical side effects such as high redox voltage, severe initial irreversible capacity, and large voltage hysteresis in the charge–discharge curves, which originate from surface-induced charge storage behavior. Therefore, intercalation-based carbon materials with superior rate and cycling performance must be developed as feasible, high-performance PIB anodes.

Disordered graphitic carbon (DGC) materials, also known as hard carbons, are composed mainly of sp²-hybridized poly-hexagonal carbon-ring structures, which include intrinsic defects such as sp³-hybridized pentagonal, heptagonal, and

^aProgram in Environmental and Polymer Engineering, Inha University, Incheon, 22212, South Korea^bKU-KIST Graduate School of Converging Science and Technology, Korea University, Seoul, 02841, South Korea^cKorea Basic Science Institute, 169-147, Daejeon, 34133, South Korea^dDepartment of Chemistry and Research Institute of Natural Sciences, Gyeongsang National University, Gyeongsangnam-do, 52828, South Korea^eInstitute of Advanced Composite Materials, Korea Institute of Science and Technology (KIST), Jeonbuk, 55324, South Korea^fDepartment of Polymer Science and Engineering, Inha University, Incheon, 22212, South Korea. E-mail: hjjin@inha.ac.kr^gDepartment of Integrative Energy Engineering, Korea University, Seoul, 02841, South Korea. E-mail: c-ysyun@korea.ac.kr

† Electronic supplementary information (ESI) available. See DOI: 10.1039/d1ta08981a

octagonal ring structures, adatoms, vacancies, and edge defects, as well as extrinsic defects.³⁶ Topological defects can cause dislocation line defects and inflict strain and pressure on adjacent carbon-ring structures, which enable the permanent deformation of the respective graphenic building blocks into tortuous shapes.³⁷ Accordingly, the graphitic lattices of hard carbons have large and irregular *d*-spacing values with poor long-range ordering, and the large potassium ions can be comfortably inserted into/extracted from the expanded graphitic lattices, which have smaller domain sizes.^{38,39} In addition, hard carbons have closed pores in their internal structure, which can mitigate the volume expansion induced by potassium-ion insertion.⁴⁰ However, hard carbons have not attracted appropriate attention as anode materials for PIBs despite these potential advantages. This could be due to the experience of lithium-ion redox chemistries, which exhibit unfavorable redox voltages and complex charge-storage mechanisms. Although several hard-carbon anodes have been developed, the relationships between the local graphitic structure and potassium-ion storage behavior have not been systematically examined. In addition, a thorough comparative study of lithium-ion and potassium-ion redox chemistries with respect to DGC materials has not been conducted.

In this study, a series of local-microstructure-tuned hard carbon samples was prepared, and the potassium-ion and lithium-ion storage behaviors of these samples were investigated and compared. Unlike the stage I lithium-ion intercalation reaction, which is observed only in highly developed graphitic structures with low *d*-spacing values of <3.46 Å, stage I potassium-ion intercalation reactions were found to mainly occur on hard carbons with poorly developed graphitic structures. Interestingly, the potassium-ion intercalation in the disordered graphitic lattices exhibited a long-range plateau capacity at a low redox voltage of ~0.1 V vs. K⁺/K, demonstrating the significant differences between the potassium-ion and previously reported lithium-ion intercalation chemistries. In addition, higher rate capabilities and highly stable cycling performances were achieved by the samples with poorly ordered graphitic structures, indicating the tremendous potential of hard carbon anodes for PIBs.

Experimental

Preparation of the DGC samples

Mulberry paper was pyrolyzed in a tube furnace from room temperature to 800 °C under a nitrogen atmosphere, at a heating rate of 10 °C min⁻¹ and holding time of 2 h at 800 °C. Subsequently, the pyrolyzed papers were thermally treated in a tube furnace at 1200 °C and 1600 °C or in a graphite furnace (ThermVac, Korea) at 2000, 2400, and 2800 °C under an Ar atmosphere. Different heating rates of 10 °C min⁻¹ up to 1600 °C, 5 °C min⁻¹ from 1600 °C to 2000 °C, and 3 °C min⁻¹ from 2000 °C to 2800 °C were applied during the high-temperature annealing, and the final temperatures were maintained for 1 h. After annealing, the furnaces were naturally cooled to room temperature, and the resulting DGC samples were stored in a vacuum oven at 30 °C.

Materials characterization

The morphologies and local microstructures of the DGC samples were examined by scanning electron microscopy (SEM; S-4300SE, Hitachi, Japan) and HRTEM (JEM2100F, JEOL, Japan). Detailed analysis of the carbon microstructures was conducted by Raman spectroscopy (LabRAM HR Evolution, HORIBA) with a laser wavelength of 514.5 nm, and XRD (Rigaku, DMAX 2500), where a Cu K α radiation generator ($\lambda = 0.154$ nm) was used in a 2θ range of 5°–60° at 100 mA and 40 kV. The surface properties of the DGC samples were analyzed by XPS using monochromatic Al K α radiation. The specific surface areas and porosities of the DGC samples were examined using the BET method based on nitrogen adsorption–desorption isotherms (ASAP 2020, Micromeritics, USA). The electrical conductivities of the pristine, lithiated, and delithiated DGC samples were measured using an electrical conductivity meter (Loresta GP, Mitsubishi Chemical, Japan).

Electrochemical characterization

The Li- and K-ion storage behavior of the DGC samples were investigated by assembling 2032-type coin cells (CR2032 type). An automatic battery cycler (WonATech) was used for the cyclic voltammetry and galvanostatic discharge/charge experiments. The coin-type half-cells were fabricated using the DGC materials as the working electrode, a glass microfiber filter as a separator, and Li or K foil as both the reference and counter electrodes. An electrolyte containing 1 M LiPF₆ ($\geq 99.99\%$, Sigma-Aldrich) or 0.8 M KPF₆ (99.5%, Sigma-Aldrich) in a 1 : 1 v/v mixed solution of EC (anhydrous 99%, Sigma-Aldrich) and DMC (anhydrous $\geq 99\%$, Sigma-Aldrich) was used in the electrochemical tests. DGC samples that were 1/2 inch in diameter were punched and directly used as working electrodes for the electrochemical analysis. For the EIS analyses, the half-cells were tested in a frequency range of 1 mHz to 0.1 MHz using an impedance analyzer (ZIVE SP2, WonATech).

Results and discussion

Traditional Korean mulberry paper (Cheongsong Hanji, Korea) was used to prepare DGCs with different local microstructures. The cellulose-based paper was found to maintain its intrinsic morphology during high-temperature annealing up to 2800 °C, and was successfully transformed into self-supporting hard carbon materials composed of bulk fibrous constituents approximately 10–20 μm in diameter (Fig. S1[†]). The free-standing bulk hard carbons were directly used for electrochemical analysis by punching them without a polymer binder, conducting carbon, or metal substrate (Fig. S2[†]), which enabled the fine analysis of their microstructure-dependent potassium-ion storage behavior.

The local microstructures of the hard carbon samples were examined by high-resolution transmission electron microscopy (HRTEM) (Fig. 1a–e and S3[†]). The HRTEM images of the samples show the gradual development of graphitic structures with increasing annealing temperature, which is indicated by the number mentioned in the sample notations. No distinctive

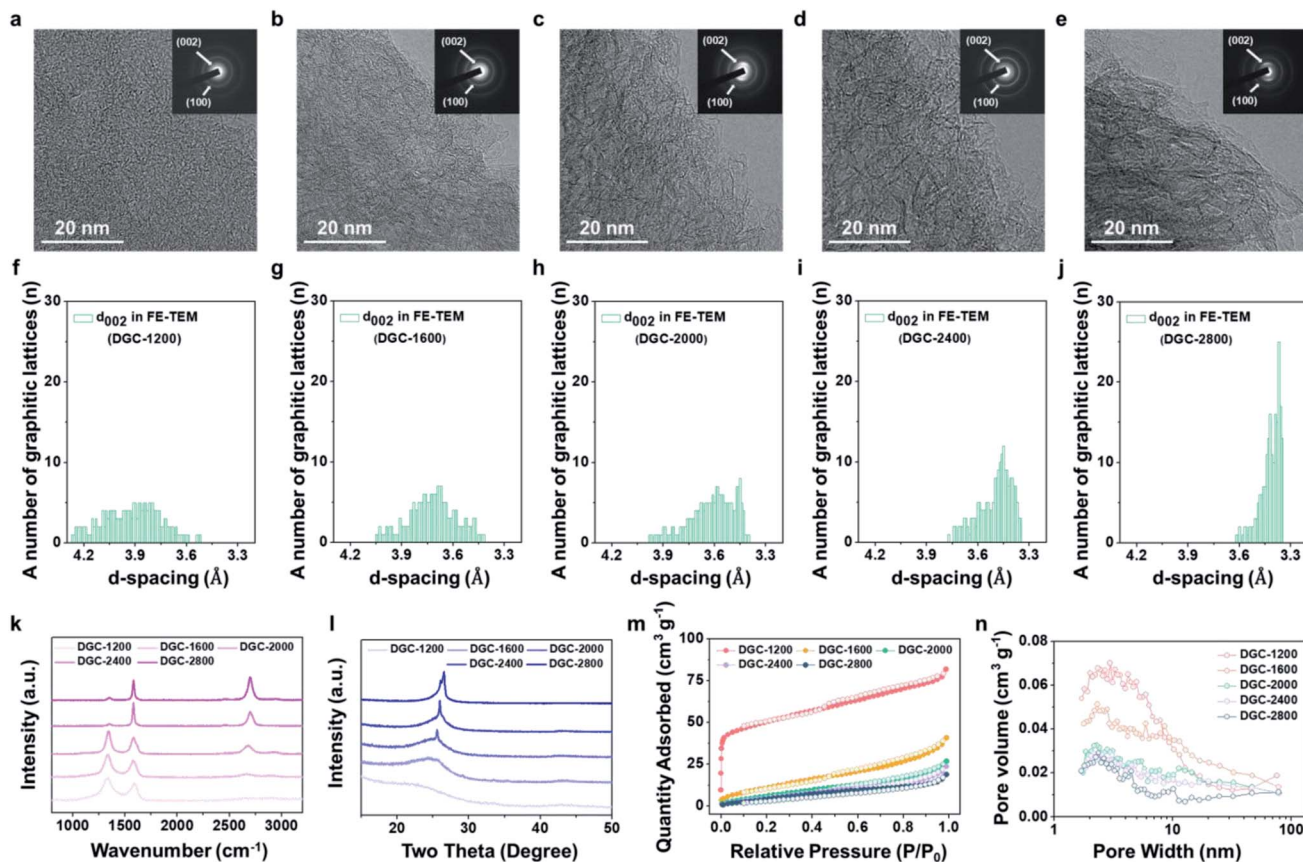


Fig. 1 Material properties of the fabricated hard carbon samples. (a–e) HRTEM images and selected area diffraction patterns, and (f–j) bar graphs showing d -spacing distributions of the DGC-1200, DGC-1600, DGC-2000, DGC-2400, and DGC-2800 samples, respectively. (k) Raman spectra, (l) XRD patterns, (m) nitrogen adsorption–desorption isotherms, and (n) pore size distribution data of the DGC samples.

graphitic lattice is visible in the HRTEM image of DGC-1200 (Fig. 1a), whereas ribbon-like lattices composed of approximately 2–6 layers are present in DGC-1600 and DGC-2000 (Fig. 1b and c); these lattices further develop into 5–15 layers in DGC-2400 and DGC-2800 (Fig. 1d and e). The overall graphitic structures appear to be randomly oriented and entangled. Additionally, the specific variations in the d -spacing of the graphitic lattices of the hard carbon samples were calculated from several TEM images, as shown in the bar graphs in Fig. 1f–j. DGC-1200 exhibits an extremely broad d -spacing variation in the range of 4.27–3.52 Å, which gradually narrows with increasing heating temperature to 4.05–3.42, 3.98–3.40, 3.77–3.35, and 3.62–3.35 Å for DGC-1600, DGC-2000, DGC-2400, and DGC-2800, respectively. Raman spectral analysis was conducted using a laser wavelength of 532 nm (Fig. 1k) to clarify these microstructural changes. All the hard carbon samples exhibit characteristic D and G bands, which originate from the A_{1g} breathing and E_{2g} vibration modes of the graphenic carbon plane, respectively; the integrated D to G intensity ratio (I_D/I_G) indicates the lateral size (L_a) of the crystalline polyhexagonal carbon domain.⁴¹ The I_D/I_G ratio does not change significantly in the spectra of the samples subjected to annealing temperatures of up to 2000 °C; the L_a values of DGCs-1200, -1600, and -2000 are ~ 2.1 , ~ 2.5 and ~ 3.4 nm, respectively. However, the D

band intensity significantly decreases at heating temperatures of ≥ 2400 °C, with the L_a values increasing up to 25.7 nm and 151.2 nm for DGC-2400 and DGC-2800, respectively. Moreover, distinctive 2D bands appear in the spectra of the samples annealed at temperatures ≥ 2000 °C. The origin of these 2D bands from three-dimensionally ordered carbon structures confirms the presence of the well-developed graphitic structures in DGC-2000, -2400, and -2800. The 2D band peak position of DGC-2000 is centered at ~ 2685 cm^{-1} , close to that of monolayer graphene, which is blue-shifted with increasing annealing temperature to ~ 2705 cm^{-1} in the spectra of the multilayered graphitic structures. This suggests the enhanced development of the ordered graphitic structures at higher annealing temperatures, which is consistent with the TEM observations. The graphitic structures were also analyzed by X-ray diffraction (XRD; Fig. 1l). The XRD pattern of DGC-1200 shows an extremely broad peak, which is closer to a mound, in the 2θ region of approximately 20° – 30° , indicating poor graphitic ordering. The broad peak narrows into a clearer shape and shifts to higher 2θ values from 25.0° (DGC-1600) to 25.4° and 25.6° for DGC-2000 and DGC-2400, respectively, with increasing annealing temperature. Moreover, an additional sharp peak appears at $\sim 25.6^\circ$ in the DGC-2000 spectrum, which increases in intensity for DGC-2400; the XRD pattern of DGC-2800 shows two split

graphitic peaks at 26.0° and 26.5°, indicating the presence of two differentiated domains in the graphitic structures. This is due to that some sp³-hybridized carbon structures, which have a stereoscopic geometry, remained in the planar graphitic domains even after the high-temperature annealing (Fig. S4†).

The porous properties of the hard carbon samples were investigated by nitrogen adsorption–desorption isotherm tests conducted at –196 °C using the Brunauer–Emmett–Teller (BET) method (Fig. 1m and n). The isotherm curves exhibit similar shapes, whereas the adsorbed quantity of nitrogen molecules decreases with increasing annealing temperature (Fig. 1m). In particular, DGC-1200 exhibits a significantly larger adsorbed quantity in the low-relative-pressure region of <0.01, which originates from the monolayer adsorption of nitrogen on the open surfaces, indicating the presence of abundant open micropores. A linear increase with relative pressure indicates the existence of a broad range of nanometer-sized pores. However, the poor hysteresis between the adsorption–desorption isotherm curves indicates the absence of distinctive mesopores; the obtained pore size distribution data support this claim (Fig. 1n). The hard carbon samples have a broad range of nanopores, which are mainly distributed below 10 nm, where the pore volume gradually decreases with increasing annealing temperature. The specific surface area of DGC-1200 (~183 m² g⁻¹) significantly decreases to ~44 m² g⁻¹ at a higher annealing temperature of 1600 °C. The specific surface area gradually decreases with annealing temperature as follows: ~183, ~44, ~29, ~24, and ~21 m² g⁻¹ at 1200, 1600, 2000, 2400, and 2800 °C, respectively.

The surface properties of the samples were analyzed by X-ray photoelectron spectroscopy (XPS; Fig. S5†). The C 1s XPS profiles confirm the presence of a major C=C bond, along with a minor C–C bond and carbon–oxygen single and double bonds. The major carbon peak gradually narrows and increases in intensity with the annealing temperature, whereas the minor peak intensities relatively decrease (Fig. S5a†). The oxygen functional groups were detected as two representative configurations (carbon–oxygen single and double bonds) in the O 1s spectra (Fig. S5b†). The C/O ratio of the samples gradually increases with annealing temperature from ~18.6 to ~128.9. The textural properties are summarized in Table S1.†

The material properties of the hard carbon samples, estimated by several analytical methods, indicate the gradual formation of polyhexagonal carbon building blocks, and the formation of densified graphitic structures with narrower *d*-spacings that have smaller open specific surface areas, with increasing annealing temperature. The systematically controlled graphitic materials were used to clarify the relationships between the local microstructure of the DGCs and their potassium-ion storage behavior by comparing them with their lithium-ion counterparts.

Electrochemical analysis of the lithium- or potassium-ion storage behavior of the hard carbon samples was conducted in an electrolyte containing 1.0 M LiPF₆ or 0.8 M KPF₆, respectively, dissolved in a 1 : 1 v/v mixed solution of ethylene carbonate (EC) and dimethyl carbonate (DMC) over voltage windows of 0.01–3.00 V vs. M⁺/M (M represents Li or K).

Cyclovoltammograms of all the hard carbon samples were obtained for both Li- and K-ion systems at a scan rate of 0.1 mV s⁻¹, and their second cycles were compared because their first cycles exhibited large irreversible capacities induced by the formation of the SEI layers (Fig. 2a and S6†). The second Li-ion cyclovoltammogram of DGC-1200 shows a gradual increase in the negative current during lithiation, where a distinctive peak is absent. In the subsequent delithiation profile, a broad oxidation peak appears at 0.25 V, and the positive current gradually decreases. The gradual increase in the negative current indicates surface-driven charge storage capacity (chemisorption) *via* a solid-solution reaction. The galvanostatic lithiation/delithiation profiles of DGC-1200 clearly exhibit single-phase charge storage behavior with no distinctive voltage plateau in the low-voltage region (<0.1 V, Fig. 2b). The second K-ion cyclovoltammogram of DGC-1200 also exhibits a similar increase in negative current during potassiation, and the Li- and K-ion cyclovoltammograms overlap, indicating that they exhibit similar chemisorption capacities (Fig. 2a). However, in the highly negative voltage region below 0.1 V, the negative current sharply increases, and a corresponding large oxidation peak appears at ~0.45 V during the subsequent depotassiation step. The clear redox peak pair indicates the intercalation of potassium ions in the equivalent graphitic lattices of DGC-1200. The galvanostatic potassiation/depotassiation profiles of DGC-1200 indicate the presence of a plateau capacity at ~0.45 V (Fig. 2c). The reversible K-ion plateau and chemisorption capacities of DGC-1200 were estimated to be ~125 mA h g⁻¹ and ~92 mA h g⁻¹, respectively, with the total capacity (~217 mA h g⁻¹) being slightly larger than its total Li-ion capacity (~196 mA h g⁻¹) (Fig. 2b and c). The lower Li-ion capacity was due to the poor plateau capacity. Additionally, in the DGC-800 which has an amorphous carbon microstructure with much higher *d*-spacing (Fig. S7†), slight higher Li-ion capacity was observed (Fig. S8†). This result suggests that Li-ion chemisorption reaction is more favorable in the not well-ordered graphitic structure. With increasing annealing temperature, the Li-ion chemisorption capacities gradually decrease, whereas the oxidation peaks and reversible plateau capacities in the cyclovoltammograms and galvanostatic profiles increase, respectively, with the exception of DGC-2800 (Fig. 2a, b, and S9†). This result suggests that the Li ions stored in the graphitic lattices of DGC-1600, -2000, and -2400 are quantitatively similar, whereas their storage mechanism gradually changes from chemisorption to intercalation reactions with the development of graphitic ordering. With respect to K-ion storage in DGC-1600, the cyclovoltammogram and galvanostatic voltage profiles exhibit a poor chemisorption capacity and a low-voltage plateau capacity that is considerably higher than that of DGC-1200 (Fig. 2a and c). It is worth noting that, despite its poor graphitic ordering, DGC-1600 exhibits a cyclovoltammogram that shows a distinctive redox peak pair, and the corresponding galvanostatic profiles exhibit a long-range plateau with a considerably low-voltage hysteresis (Fig. 1b, g, k, and l). Similar voltage plateaus are exhibited by the samples prepared at higher annealing temperatures; however, the reversible plateau capacities gradually decrease with

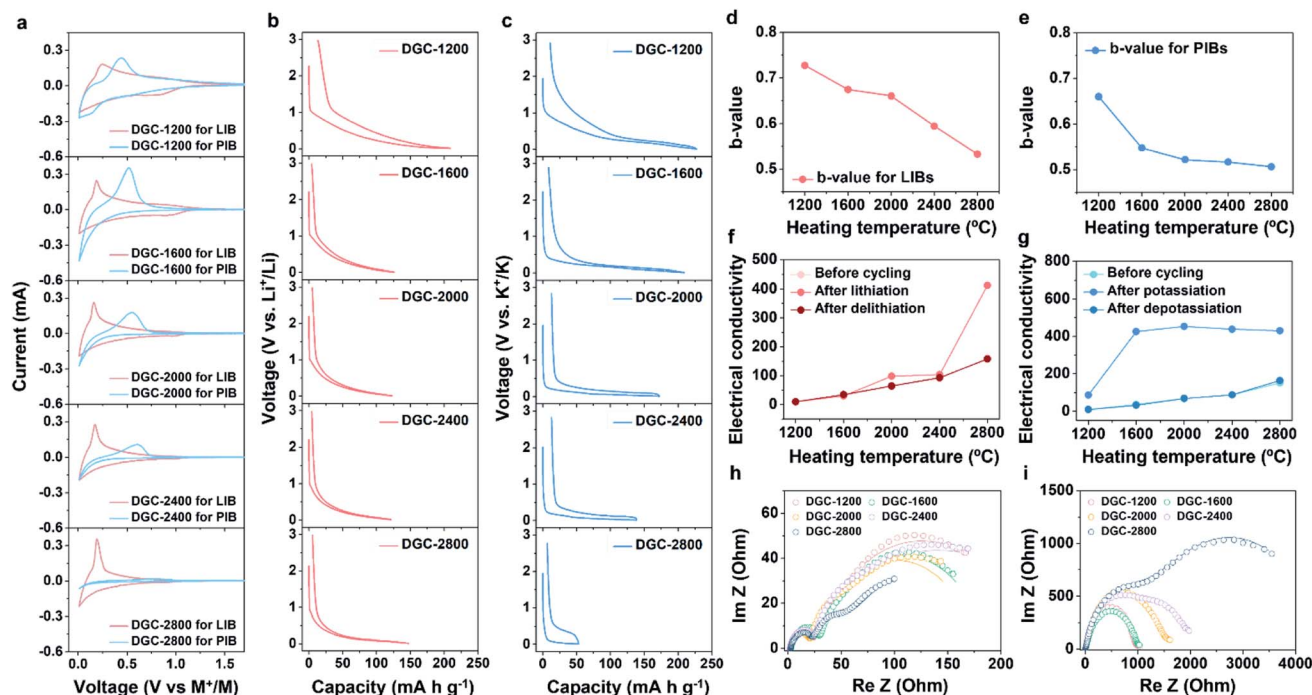


Fig. 2 Electrochemical analysis of lithium- and potassium-ion storage behavior of the hard carbon samples. (a) Cyclic voltammograms obtained at a scan rate of 0.1 mV s^{-1} in different alkali-cation charge carriers, and galvanostatic discharge/charge profiles acquired over a voltage window of $0.01\text{--}3.00 \text{ V vs. M}^+/\text{M}$ in electrolytes of (b) 1.0 M LiPF_6 and (c) 0.8 M KPF_6 dissolved in a $1 : 1 \text{ v/v}$ mixed solution of EC/DMC at a current density of 20 mA g^{-1} . The b -value distribution data obtained in the (d) lithium- and (e) potassium-ion systems. Electrical conductivities of (f) pristine, lithiated and, delithiated DGC samples, and (g) pristine, potassiated, and depotassiated DGC samples. EIS profiles and fitting curves of (h) lithiated and (i) potassiated DGC samples obtained after the 10^{th} cycle.

increasing annealing temperature (Fig. 2a and c). As shown in Fig. S10,[†] the dQ/dV curves support the antithetic redox behavior of the hard carbon samples in the different charge-carrier systems. The Li-ion dQ/dV curve of only DGC-2800 shows sharp redox peaks originating from the intercalation reaction stages in the low-voltage region, indicating that the other samples primarily store Li ions *via* chemisorption. These results suggest that the Li-ion intercalation reaction is remarkably sensitive to graphitic ordering because a slight expansion of the d -spacing alters the Li-ion storage mechanism. In contrast, the K-ion dQ/dV curves of DGC-1600, -2000, and -2400 show high-intensity peak pairs in the low-voltage region, although these samples exhibit significantly different graphitic ordering, particularly between DGC-2000 and DGC-2400. The intercalation capacities gradually decrease with the development of graphitic ordering, which is an incomprehensible behavior in terms of typical Li-ion storage chemistries. Moreover, the poorly ordered hard carbon, DGC-1600, exhibits the highest reversible dQ/dV peak intensity of all the hard carbon samples.

Further electrochemical analysis was conducted to elucidate this unusual K-ion storage mechanism (Fig. 2d and e). According to the equation, $i = av^b$, where a and b are adjustable values, the peak current (i) and scan rate (v) follow a simple power law.⁴² The value of b approaches 0.5 or 1.0 when the mechanism of charge storage is diffusion-controlled or surface-controlled, respectively. In terms of graphitic materials, the diffusion-

controlled charge storage behavior indicates the occurrence of intercalation reactions in the equivalent redox sites, whereas the surface-controlled charge storage behaviors represent pseudocapacitive reactions *via* a solid-solution mechanism.⁴³ The hard carbon samples exhibit a gradual decrease in the estimated values of b for Li-ion storage (Fig. S11[†]) with increasing annealing temperature, from 0.73 for DGC-1200 to 0.67, 0.66, 0.59, and 0.53 for DGC-1600, -2000, -2400, and -2800, respectively (Fig. 2d). This suggests that the Li-ion storage behavior proceeds *via* the surface-controlled mechanism mixed with a diffusion-controlled character, which becomes more dominant with increasing annealing temperature. In contrast, similar values of b are obtained for DGC-1600, DGC-2000, DGC-2400, and DGC-2800 in terms of K-ion storage (0.55, 0.52, 0.52, and 0.51, respectively), regardless of their different microstructures (Fig. 2e and S12[†]). The diffusion-controlled K-ion storage mechanism indicates that the K-ion intercalation reaction can occur in poorly ordered graphitic structures. This is in contrast to the Li-ion intercalation reaction, which is highly sensitive to local graphitic ordering.

The intercalation behavior can be traced using changes in the electrical conductivity because of the significant influence of alkali-ion intercalants on the electronic properties of graphitic materials.^{44,45} As shown in Fig. 2f, the electrical conductivity of DGC-2800 significantly increases with lithiation from $\sim 160 \text{ S cm}^{-1}$ to $\sim 415 \text{ S cm}^{-1}$, whereas those of the other samples are unaffected by lithiation; moreover, the electrical

conductivity reversibly returns to its initial value after delithiation. This result implies that only DGC-2800 stores Li ions *via* an intercalation-dominated reaction mechanism. In contrast, the electrical conductivities of all the samples, except for DGC-1200, increase in the 425–455 S cm⁻¹ range with potassiation and reversibly revert to their initial values after depotassiation, supporting the assertion that the DGC materials prepared at annealing temperatures of ≥ 1600 °C primarily store K ions *via* an intercalation mechanism (Fig. 2g).

Optical images of the hard carbon samples can also demonstrate the intercalation behavior based on their color changes (Fig. 3). Stage I intercalation compounds are known to have a golden color, whereas the stage II, III, and IV intercalation compounds exhibit a blue color.^{46,47} The optical images of the fully lithiated hard-carbon samples reveal that the metallic silver gray colored pristine sample transforms into dark blue (almost black) DGC-1200 and DGC-1600 (Fig. 3a, b, S2a, and b†), pure blue DGC-2000 and DGC-2400 (Fig. 3c, d, S2c, and d†), and dark gold DGC-2800 (Fig. 3e and S2e†). This result indicates the considerable enhancement in the Li-ion intercalation reactions with annealing temperature, and the partial formation of a stage I intercalation compound corresponding to LiC₆ in DGC-2800, which adequately agrees with the results obtained by the electrochemical analyses shown in Fig. 2. In addition, the fully potassiated DGC-1600 and DGC-2000 samples exhibit dark orange colors, which indicates that the intercalation compounds are primarily composed of a stage I intercalation compound corresponding to KC₈ (Fig. 3g, h, S2b and c†). In contrast, the highly ordered DGC-2400 and DGC-2800 samples appear blue and black, respectively, indicating their poor intercalation behavior (Fig. 3i, j, S2d and e†). Therefore, the results obtained by the various electrochemical tests and the variations in electrical conductivity and color consistently indicate that the DGC materials with poor local ordering can store K ions *via* intercalation at a low voltage of ~ 0.1 V. However, the large K-ion intercalation behavior could be hampered by the growth of the disordered graphitic structures because the K-ion intercalation inevitably induces a large volume expansion ($\sim 160\%$), while the complicated interconnected graphitic domains restrict the volumetric expansion of the graphitic lattices. The electrochemical impedance spectroscopy (EIS) data confirmed this expectation (Fig. 2h and i). The EIS profiles of the fully lithiated samples show two semicircles corresponding to the surface film resistance (R_f) and charge-transfer resistance (R_{ct}), where the R_{ct} value of DGC-2800, which exhibits the intercalation-dominated reaction mechanism, is considerably lower than those of the other samples (Fig. 2h). This indicates that lithiation is more favorable in hard carbon samples with highly ordered graphitic structures. In contrast, the EIS profiles of the fully potassiated samples exhibit a larger semicircle featuring R_f mixed with R_{ct} , where the semicircle diameter increases with increasing annealing temperature (Fig. 2i). In particular, the R_{ct} value of DGC-2800 is significantly larger than those of the others, indicating the considerable hindering of K-ion delivery into the interior of DGC-2800. This result suggests that the poor K-ion

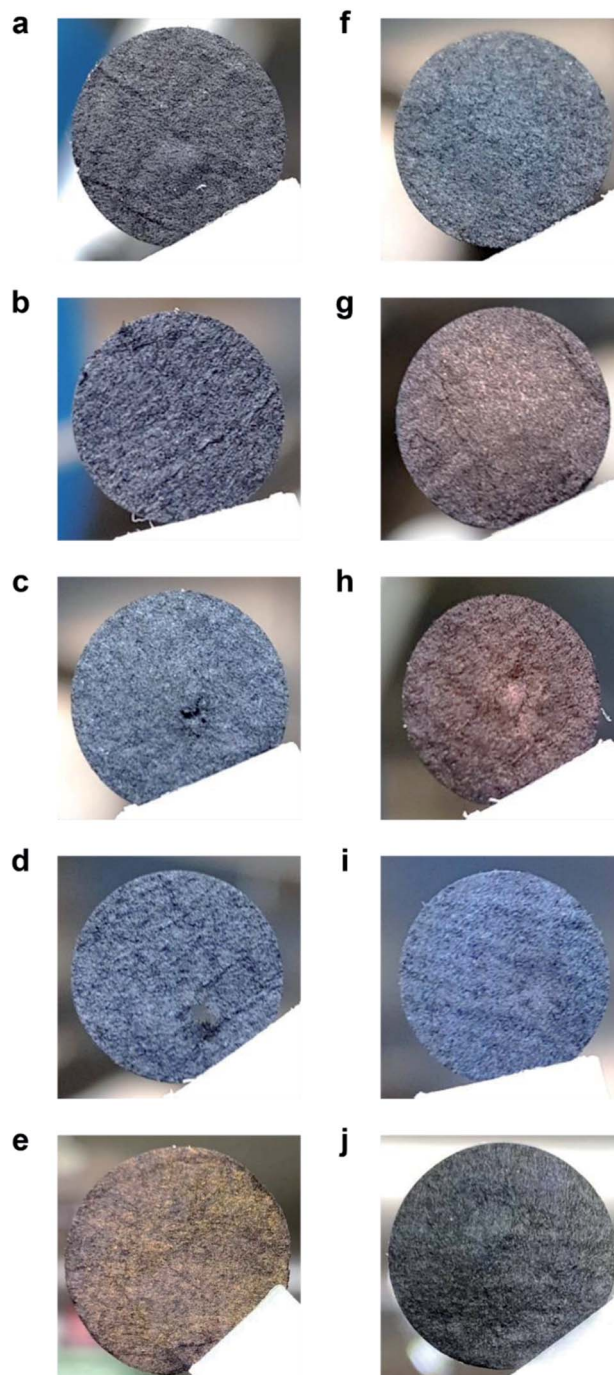


Fig. 3 Optical images showing lithiation- and potassiation-induced color changes: (a–e) lithiated and (f–j) potassiated DGC-1200, DGC-1600, DGC-2000, DGC-2400, and DGC-2800 samples, respectively.

plateau capacity of DGC-2800 is due to kinetic limitations rather than the absence of redox active sites.

More importantly, the K-ion intercalation reaction on a DGC material with poor local graphitic ordering progresses without the formation of a new intercalation phase, as shown in the *in situ* XRD patterns of DGC-1600 obtained at the 2nd and 3rd potassiation/depotassiation cycles (Fig. 4a). During potassiation, the broad graphite (002) peak becomes increasingly

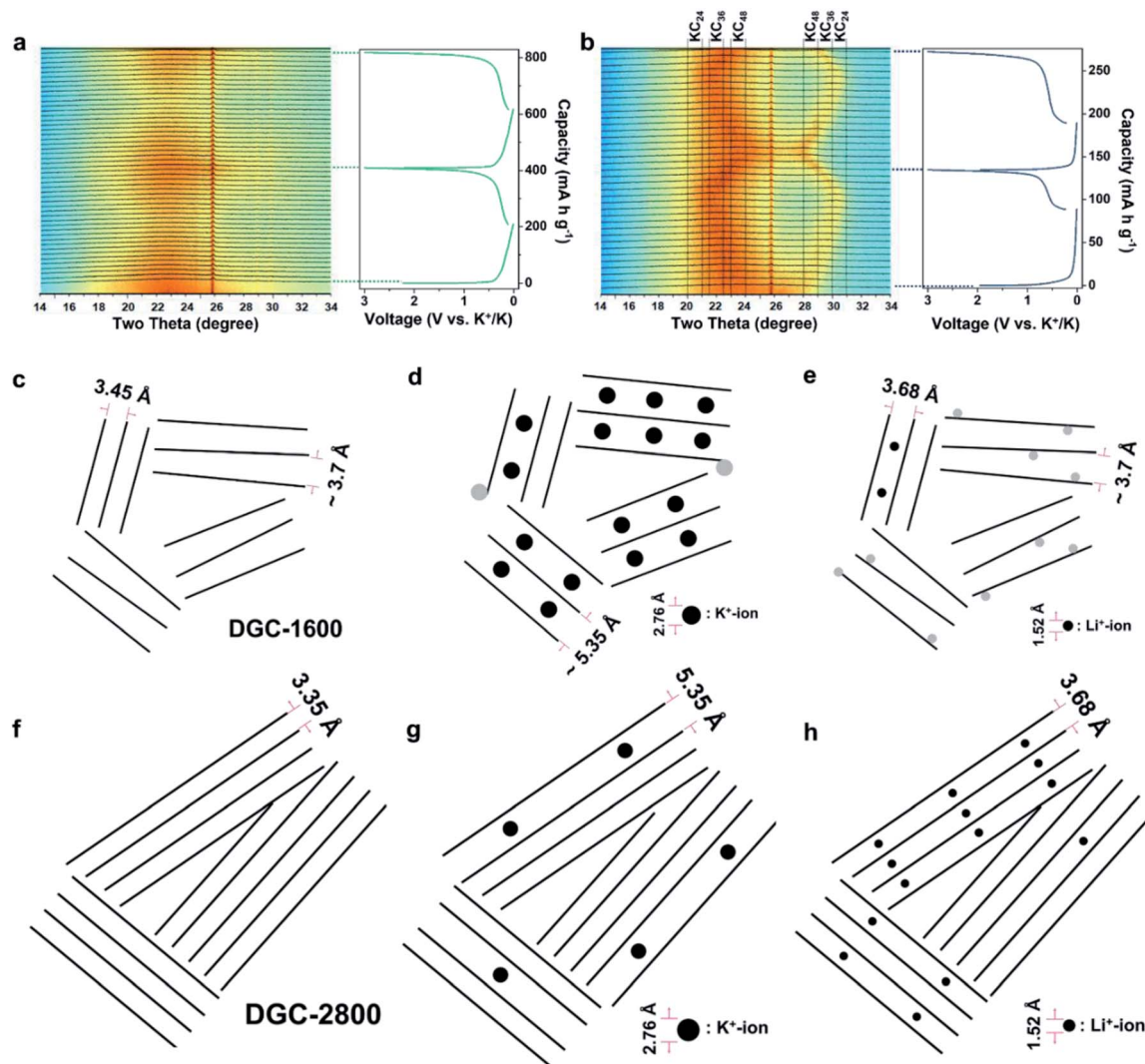


Fig. 4 *In situ* XRD patterns of (a) DGC-1600 and (b) DGC-2800 with galvanostatic discharge/charge profiles, and illustrations showing the intercalation behavior of (c) pristine DGC-1600, (d) potassiated DGC-1600, (e) lithiated DGC-1600, (f) pristine DGC-2800, (g) potassiated DGC-2800, and (h) lithiated DGC-2800.

amorphized, and recovers during the subsequent depot-assiation, indicating a solid-solution intercalation reaction. This single-phase K-ion intercalation behavior is remarkably different from the previously reported intercalation mechanism in graphite-based materials.^{48,49} In contrast, the DGC-2800 sample, with its highly ordered local graphitic ordering, exhibits typical two-phase intercalation behavior that form stages IV, III, and II (Fig. 4b). The limited K-ion charge carriers are intercalated in the graphitic lattices owing to the presence of these complicated local microstructures, whereas the high-capacity stage I compounds are absent. In addition to their poor capacity, the highly developed hard carbons also exhibit poor rate capabilities and cycling stabilities (Fig. S13[†]). An increase in the current density up to 150 mA g^{-1} resulted in the reversible capacities of DGC-2800 converging to nearly zero, whereas those of DGC-1600 maintained approximately 70% of their initial capacity at a high current density of 150 mA g^{-1} (Fig. S13a[†]). In addition, DGC-1600 exhibits a highly stable

capacity retention during the cycling test conducted over 100 cycles, whereas DGC-2800 exhibits a large capacity fluctuation (Fig. S13b[†]). *Ex situ* HRTEM image of DGC-1600 characterized after 10^{th} cycle shows the similar carbon microstructure to the pristine DGC-1600 before cycling, supporting the cycling stability (Fig. S14[†]). Table S3[†] exhibits electrochemical performances of the previously reported DGC materials as an anode for potassium ion storage.^{6,50–58} Although the test condition and electrode configuration are different each other, DGC-1600 shows relatively high initial coulombic efficiency and good cycling retention in the listed DGC materials. Moreover, most of the reported DGC materials show feasible potassium ion storage performances despite their large *d*-spacing, supporting our claim that the solid-solution intercalation-based DGC materials can be a suitable anode for potassium ion batteries.

To further support feasibility of DGC-1600 which has the highest electrochemical performances in the tested DGC samples, a full cell test with a nanostructured graphite cathode

(NGC) was conducted.⁵⁹ In a half cell test for the NGC over a voltage window between 3.0–5.3 V vs. K⁺/K, a specific capacity of ~60 mA h g⁻¹ was reversibly achieved in the high voltage range (Fig. S15a†). When the DGC-1600 and NGC were assembled as anode and cathode, respectively, in the full cell, a reversible capacity of ~40 mA h g⁻¹ and an average voltage of ~4.5 V were achieved (Fig. S15b†). This corresponds to a specific energy density of ~180 W h kg⁻¹ at a specific power density of ~450 W kg⁻¹ (Fig. S15c†). Although the specific energy densities were gradually decreased with increasing specific power densities, the Ragone plot of the DGC-1600//NGC full cell occupies the right upper end sites compared with them of the previously reported full cells.^{60–65} This indicates the higher energy and power performances of the DGC-1600//NGC full cell. In addition, the full cell reversibly worked over 100 cycles, and a capacity retention of >80% was attained after 100th cycle (Fig. S15d†).

Conclusions

A comparative study of a series of hard carbon samples with systematically controlled local graphitic microstructures was conducted, which revealed that the stage I K-ion intercalation reaction can occur in highly disordered graphitic structures with a few nanometer-sized graphitic domains and an expanded *d*-spacing of >3.5 Å (Fig. 4c and d). This behavior is unusual in terms of typical Li-ion intercalation chemistries because the Li-ion intercalation mechanism is extremely sensitive to the graphitic microstructure. When Li ions are intercalated in these disordered graphitic structures, most of the charges are stored *via* chemisorption (Fig. 4c and e). However, the larger K-ion intercalation reaction is physically limited by the development of the graphitic ordering of the hard carbon materials because of the significantly increased charge-transfer resistance, resulting in a poor intercalation capacity (Fig. 4f and g). This is antithetic to the Li-ion intercalation behavior that becomes more favorable with the growth of the graphitic structures of the hard carbon materials (Fig. 4f and h).

Conflicts of interest

There are no conflicts to declare.

Acknowledgements

This research was supported by the Basic Science Research Program through the National Research Foundation of Korea (NRF) funded by the Ministry of Education (NRF-2019R1A2C1084836, and NRF-2021R1A4A2001403). This work was supported by the KU-KIST School Program.

Notes and references

- 1 M. Armand and J.-M. Tarascon, *Nature*, 2008, **451**, 652–657.
- 2 M. Li, J. Lu, X. Ji, Y. Li, Y. Shao, Z. Chen, C. Zhong and K. Amine, *Nat. Rev. Mater.*, 2020, **5**, 276–294.

- 3 Y. Li, Y. Lu, P. Adelhelm, M. M. Titirici and Y. S. Hu, *Chem. Soc. Rev.*, 2019, **48**, 4655–4687.
- 4 N. Xia, W. D. McCulloch and Y. Wu, *J. Am. Chem. Soc.*, 2017, **139**, 9475–9478.
- 5 N. S. Katorova, S. S. Fedotov, D. P. Rupasov, N. D. Luchinin, B. Delattre, Y.-M. Chiang, A. M. Abakumov and K. J. Stevenson, *ACS Appl. Energy Mater.*, 2019, **2**, 6051–6059.
- 6 L. Fan, S. Chen, R. Ma, J. Wang, L. Wang, Q. Zhang, E. Zhang, Z. Liu and B. Lu, *Small*, 2018, **14**, 1801806.
- 7 H. Wang, D. Zhai and F. Kang, *Energy Environ. Sci.*, 2020, **13**, 4583.
- 8 N. S. Katorova, S. Y. Luchkin, D. P. Rupasov, A. M. Abakumov and K. J. Stevenson, *J. Chem. Phys.*, 2020, **152**, 194704.
- 9 C. Zhang, Y. Xu, M. Zhou, L. Liang, H. Dong, M. Wu, Y. Yang and Y. Lei, *Adv. Funct. Mater.*, 2017, **27**, 1604307.
- 10 A. Eftekhari, *J. Power Sources*, 2004, **126**, 221–228.
- 11 K. Beltrop, S. Beuker, A. Heckmann, M. Winter and T. Placke, *Energy Environ. Sci.*, 2017, **10**, 2090–2094.
- 12 K. Chihara, A. Katogi, K. Kubota and S. Komaba, *Chem. Commun.*, 2017, **53**, 5208.
- 13 G. Wang, M. Yu, J. Wang, D. Li, D. Tan, M. Löffler, X. Zhuang, K. Müllen and X. Feng, *Adv. Mater.*, 2018, **30**, 1800533.
- 14 J. Liao, C. Chen, Q. Hu, Y. Du, Y. He, Y. Xu, Z. Zhang and X. Zhou, *Angew. Chem., Int. Ed.*, 2021, **60**, 25575–25582.
- 15 L. Duan, Y. Xu, Z. Zhang, J. Xu, J. Liao, J. Xu, Y. Sun, Y. He and X. Zhou, *J. Mater. Chem. A*, 2021, **9**, 22820–22826.
- 16 X. Chang, X. Zhou, X. Ou, C.-S. Lee, J. Zhou and Y. Tang, *Adv. Energy Mater.*, 2019, **9**, 1902672.
- 17 H. Yamamoto, S. Muratsubaki, K. Kubota, M. Fukunishi, H. Watanabe, J. Kim and S. Komaba, *J. Mater. Chem. A*, 2018, **6**, 16844.
- 18 D.-S. Bin, X.-J. Lin, Y.-G. Sun, Y.-S. Xu, K. Zhang, A.-M. Cao and L.-J. Wan, *J. Am. Chem. Soc.*, 2018, **140**, 7127–7134.
- 19 W. Yang, J. Zhou, S. Wang, W. Zhang, Z. Wang, F. Lv, K. Wang, Q. Sun and S. Guo, *Energy Environ. Sci.*, 2019, **12**, 1605–1612.
- 20 B. Wang, F. Yuan, W. Li, Q. Wang, X. Ma, L. Gu, H. Sun, K. Xi, D. Zhang and W. Wang, *Nano Energy*, 2020, **75**, 104979.
- 21 Y. Qian, Y. Li, Z. Yi, J. Zhou, Z. Pan, J. Tian, Y. Wang, S. Sun, N. Lin and Y. Qian, *Adv. Funct. Mater.*, 2021, **31**, 2006875.
- 22 K. Share, A. P. Cohn, R. Carter, B. Rogers and C. L. Pint, *ACS Nano*, 2016, **10**, 9738–9744.
- 23 W. Zhang, J. Mao, S. Li, Z. Chen and Z. Guo, *J. Am. Chem. Soc.*, 2017, **139**, 3316–3319.
- 24 W. Zhang, Z. Cao, W. Wang, E. Alhajji, A.-H. Emwas, P. M. F. J. Costa, L. Cavallo and H. N. Alshareef, *Angew. Chem., Int. Ed.*, 2020, **59**, 4448–4455.
- 25 W. Li, D. Wang, Z. Gong, X. Guo, J. Liu, Z. Zhang and G. Li, *Carbon*, 2020, **161**, 97–107.
- 26 J. Li, Y. Li, X. Ma, K. Zhang, J. Hu, C. Yang and M. Liu, *Chem. Eng. J.*, 2020, **384**, 123328.
- 27 L. Tao, Y. Yang, H. Wang, Y. Zheng, H. Hao, W. Song, J. Shi, M. Huang and D. Mitlin, *Energy Storage Mater.*, 2020, **27**, 212–225.
- 28 Z. Xu, S. Du, Z. Yi, J. Han, C. Lai, Y. Xu and X. Zhou, *ACS Appl. Energy Mater.*, 2020, **3**, 11410–11417.

- 29 Y. Du, W. Weng, Z. Zhang, Y. He, J. Xu, J. Sun, J. Liao, J. Bao and X. Zhou, *ACS Mater. Lett.*, 2021, **3**, 356–363.
- 30 W. Weng, J. Xu, C. Lai, Z. Xu, Y. Du, J. Lin and X. Zhou, *J. Alloys Compd.*, 2020, **817**, 152732.
- 31 C. Lai, Z. Zhang, Y. Xu, J. Liao, Z. Xu, Z. Yi, J. Xu, J. Bao and X. Zhou, *J. Mater. Chem. A*, 2021, **9**, 1487–1494.
- 32 J. Zhao, X. Zou, Y. Zhu, Y. Xu and C. Wang, *Adv. Funct. Mater.*, 2016, **26**, 8103–8110.
- 33 L. Fan, R. Ma, Q. Zhang, X. Jia and B. Lu, *Angew. Chem., Int. Ed.*, 2019, **58**, 10500–10505.
- 34 W. Wang, J. Zhou, Z. Wang, L. Zhao, P. Li, Y. Yang, C. Yang, H. Huang and S. Guo, *Adv. Energy Mater.*, 2018, **8**, 1701648.
- 35 J. Chen, Y. Cheng, Q. Zhang, C. Luo, H.-Y. Li, Y. Wu, H. Zhang, X. Wang, H. Liu, X. He, J. Han, D.-L. Peng, M. Liu and M.-S. Wang, *Adv. Funct. Mater.*, 2021, **31**, 2007158.
- 36 S. Y. Cho, Y. S. Yun, D. Jang, J. W. Jeon, B. H. Kim, S. Lee and H.-J. Jin, *Nat. Commun.*, 2017, **8**, 74.
- 37 A. Oberlin, *Carbon*, 1984, **22**, 521–541.
- 38 J. Chen, B. Yang, H. Hou, H. Li, L. Liu, L. Zhang and X. Yan, *Adv. Energy Mater.*, 2019, **9**, 1803894.
- 39 Y. Jiang, Y. Yang, R. Xu, X. Cheng, H. Huang, P. Shi, Y. Yao, H. Yang, D. Li, X. Zhou, Q. Chen, Y. Feng, X. Rui and Y. Yu, *ACS Nano*, 2021, **15**, 10217–10227.
- 40 S. U. Yoon, H. Kim, H.-J. Jin and Y. S. Yun, *Appl. Surf. Sci.*, 2021, **547**, 149193.
- 41 M. E. Lee, S. M. Lee, J. Choi, D. Jang, S. Lee, H.-J. Jin and Y. S. Yun, *Small*, 2020, **16**, 2001053.
- 42 V. Augustyn, J. Come, M. A. Lowe, J. W. Kim, P.-L. Taberna, S. H. Tolbert, H. D. Abruña, P. Simon and B. Dunn, *Nat. Mater.*, 2013, **12**, 518–522.
- 43 X. Hu, Y. Liu, J. Chen, L. Yi, H. Zhan and Z. Wen, *Adv. Energy Mater.*, 2019, **9**, 1901533.
- 44 D. M. Ottmers and H. F. Rase, *Carbon*, 1966, **4**, 125–127.
- 45 W. Bao, J. Wan, X. Han, X. Cai, H. Zhu, D. Kim, D. Ma, Y. Xu, J. N. Munday, H. D. Drew, M. S. Fuhrer and L. Hu, *Nat. Commun.*, 2014, **5**, 4224.
- 46 Y. Wang, P. Puech, I. Gerber and A. Pénicaud, *J. Raman Spectrosc.*, 2014, **45**, 219–223.
- 47 M. Drüe, M. Seyring and M. Rettenmayr, *J. Power Sources*, 2017, **353**, 58–66.
- 48 J. Yang, Y. Zhai, X. Zhang, E. Zhang, H. Wang, X. Liu, F. Xu and S. Kaskel, *Adv. Energy Mater.*, 2021, **11**, 2100856.
- 49 J. Liu, T. Yin, B. Tian, B. Zhang, C. Qian, Z. Wang, L. Zhang, P. Liang, Z. Chen, J. Yan, X. Fan, J. Lin, X. Chen, Y. Huang, K. P. Loh and Z. X. Shen, *Adv. Energy Mater.*, 2019, **9**, 1900579.
- 50 Y. Feng, S. Chen, D. Shen, J. Zhou and B. Lu, *Energy Environ. Mater.*, 2021, **4**, 451–457.
- 51 X. Zhao, Y. Tang, C. Ni, J. Wang, A. Star and Y. Xu, *ACS Appl. Energy Mater.*, 2018, **1**, 1703–1707.
- 52 Z. Jian, Z. Xing, C. Bommier, Z. Li and X. Ji, *Adv. Energy Mater.*, 2016, **6**, 1501874.
- 53 J. Yang, Z. Ju, Y. Jiang, Z. Xing, B. Xi, J. Feng and S. Xiong, *Adv. Mater.*, 2018, **30**, 1700104.
- 54 C. Fan, M. Ou, P. Wei, J. Xu, S. Sun, Y. Liu, Y. Xu, C. Fang, Q. Li and J. Han, *RSC Adv.*, 2021, **11**, 14883–14890.
- 55 Z. Li, W. Shin, Y. Chen, J. C. Neuefeind, P. A. Greaney and X. Ji, *ACS Appl. Energy Mater.*, 2019, **2**, 4053–4058.
- 56 R. Hao, H. Lan, C. Kuang, H. Wang and L. Guo, *Carbon*, 2018, **128**, 224–230.
- 57 Z. Wu, J. Zou, Y. Zhang, X. Lin, D. Fry, L. Wang and J. Liu, *Chem. Eng. J.*, 2022, **427**, 131547.
- 58 X. Lin, J. Huang and B. Zhang, *Carbon*, 2019, **143**, 138–146.
- 59 Y. S. Yun, *Nanoscale Res. Lett.*, 2018, **13**, 36.
- 60 J. Zhu, Y. Li, B. Yang, L. Liu, J. Li, X. Yan and D. He, *Small*, 2018, **14**, 1801836.
- 61 X. Ding, F. Zhang, B. Ji, Y. Liu, J. Li, C.-S. Lee and Y. Tang, *ACS Appl. Mater. Interfaces*, 2018, **10**, 42294–42300.
- 62 D. Qiu, J. Guan, M. Li, C. Kang, J. Wei, Y. Li, Z. Xie, F. Wang and R. Yang, *Adv. Funct. Mater.*, 2019, **29**, 1903496.
- 63 S. Dong, Z. Li, Z. Xing, X. Wu, X. Ji and X. Zhang, *ACS Appl. Mater. Interfaces*, 2018, **10**, 15542–15547.
- 64 B. Ji, F. Zhang, X. Song and Y. Tang, *Adv. Mater.*, 2017, **29**, 1700519.
- 65 L. Fan, Q. Liu, S. Chen, K. Lin, Z. Xu and B. Lu, *Small*, 2017, **13**, 1701011.